JOURNAL OF APPLIED PHYSICS VOLUME 94, NUMBER 9 1 NOVEMBER 2003

Size effects on the onset of plastic deformation during nanoindentation of thin films and patterned lines

Yoonjoon Choi
Department of Materials Science and Engineering, Massachusetts Institute of Technology, Cambridge, Massachusetts 02139

Krystyn J. Van Vliet
Department of Surgical Research, Children's Hospital and Harvard Medical School, Boston, Massachusetts 02115

Ju Li
Department of Materials Science and Engineering, Ohio State University, Columbus, Ohio 43210

Subra Suresh[a)]
Department of Materials Science and Engineering, Massachusetts Institute of Technology, Cambridge, Massachusetts 02139

(Received 28 April 2003; accepted 13 August 2003)

Plastic deformation of materials exhibits a strong size dependence when the relevant physical length scales are in the range of microns or below. Recent progress in experimental and computational nanoindentation allows us to investigate the mechanical response of nanoscale material volumes, particularly the transition from elastic to plastic deformation and the early stages of plastic deformation. We present a systematic experimental study of nanoindentation on continuous films and unidirectionally patterned lines on substrates to explore the effects of two size scales (film thickness *t* and linewidth *w*) on the early stages of plastic deformation via the investigation of the nanoindentation $P-h$ response. The observed experimental trends indicate that early stage plasticity is strongly size dependent, a feature that cannot be rationalized on the basis of continuum concepts. Computational simulations of these nanoindentation experiments through finite element modeling and molecular dynamics are conducted to elucidate the mechanisms by which this incipient plasticity progresses in the material by correlating observations from both experiments and computations. © *2003 American Institute of Physics.* [DOI: 10.1063/1.1615702]

I. INTRODUCTION

The deformation of materials occurs via two distinct processes: elastic (reversible) and plastic (irreversible) deformation. Since elastic deformation is a reversible process, and is governed by angstrom scale (10^{-10} m) interaction parameters such as the crystallographic lattice constants, elastic deformation of materials exhibits virtually no size dependence unless a large population of preexisting defects is involved.[1,2] Conversely, it has been established that physical and microstructural length scales exert a strong influence on the plastic deformation behavior of materials, as a consequence of the coupling between two competing size parameters:[3,4] the fundamental length scale of the physical phenomena involved (e.g., the mean-free path and distance among dislocations, in the case of plasticity) and the structural dimensions of the material (e.g., grain size, film thickness, and linewidth). The plastic deformation response, which occurs as a result of the generation, annihilation, and motion of defects such as dislocations, displays marked size effects when those material dimensions are in the range of microns or below.

The controlling mechanisms of plastic deformation in metallic materials, as well as the size dependence of this deformation, have been topics of long-standing scientific interest.[3] In addition, the technological relevance of this issue as it relates to microelectronic thin films has generated a large research effort over the last decade.[5,6] Recent progress in nanoindentation allows us to investigate the deformation behavior of materials at the nanoscale, particularly the transition from elastic to plastic deformation and the early stages of plastic deformation. The characteristics of such experimental results are summarized as follows:[7–9] (i) The initial load–displacement $(P-h)$ response is elastic and can be described by continuum level contact mechanics. (ii) The first departure from this elastic response occurs when the local maximum shear stress level sustained by the indented material is on the order of the theoretical shear strength of material (i.e., the stress required to nucleate a dislocation homogeneously). (iii) Subsequent to this initial plastic event, a series of similar discontinuities in the $P-h$ response occurs. Although the fundamental mechanisms responsible for the experimentally observed discrete deformation processes under this nanoscale contact are still debated in the literature, recent experimental and computational studies[10,11] have shown that the initiation of such discrete plasticity is related to the homogeneous nucleation mechanism of defects, where new defects (chiefly dislocations) are nucleated in the crystal due to the elastic instability induced via contact loading.

In this study, we present a systematic experimental study of nanoindentation on continuous thin films and unidirectionally patterned unpassivated lines of Al on Si substrates to

---

[a)] Electronic mail: ssuresh@mit.edu

explore the effects of two size scales (film thickness t and linewidth w) on the early stage of plastic deformation via the investigation of the nanoindentation $P-h$ response. Although both the film and the line are constrained at the substrate interface in the same manner, the film extends infinitely in both in-plane directions, whereas the line extends infinitely along only one in-plane axis and is unconstrained in the orthogonal in-plane direction (i.e., unconstrained normal to the line sidewalls). The observed experimental trends exhibit a strong size dependence, which cannot be rationalized on the basis of continuum concepts and suggest a significant effect of these boundary conditions on the plastic deformation mechanism. Continuum and atomistic computational simulations of these nanoindentation experiments through finite element modeling (FEM) and molecular dynamics (MD), respectively, are conducted to elucidate the mechanism by which constraint influences the size dependence of plastic flow, as well as the mechanisms by which this earliest stage of plastic deformation progresses in the material. By correlating observations from both experiments and computations, possible mechanisms responsible for those size effects are discussed.

II. EXPERIMENTS

A. Materials and experimental procedures

Polycrystalline thin films of Al–1.5 wt% Si, 0.33, 0.7, and 1.0 μm in thickness, were sputter deposited onto 525-μm-thick Si substrates at room temperature. X-ray diffraction data confirmed a strong {111}-oriented texture of all films. Transmission electron microscopy (TEM) of an as-deposited film of 1 μm thickness showed that the average grain size of the film was ~0.6 μm and that the grains exhibited a typical columnar structure. A film of 1 μm thickness was subsequently patterned into sets of parallel lines with different widths, using standard photolithography and dry etching techniques. The nominal linewidth w was varied from 1.5 to 5.0 μm with an incremental increase in width of 0.5 μm, for a total number of eight linewidth sets of seven lines each, with an interline spacing equal to w and interset spacing of 20 μm. The length of each line was 500 μm. A square pad of 500 μm×500 μm was patterned next to the sets of lines to represent a continuous thin film. All structures were constructed on the same wafer by a single set of deposition and etching processes such that all characteristics of film and lines are expected to be the same, except for the in-plane dimensional length scale (i.e., linewidth w).

Nanoindentation experiments were carried out with three-sided diamond Berkovich indenter tips on two commercially available nanoindenters: NanoTest600 (MicroMaterials, LLC, Wrexham, U.K.) and Triboindenter (Hysitron, Inc., Minneapolis, MN). Each apparatus was instrumented with an indenter of a particular radius. The tip radii (R) were experimentally verified as ~500 nm (NanoTest600) and ~100 nm (Triboindenter), using shallow (elastic) indentations on quartz and the analytical Hertzian solution of spherical indentations.[12] All necessary experimental parameters, such as the tip area function and frame compliance, were calibrated prior to each set of experiments using a standard quartz specimen on both nanoindenters, according to the extrapolation method of Oliver and Pharr.[13] Load-controlled nanoindentations were conducted over a complete loading and unloading cycle on both the films and lines. On the NanoTest600, loading was terminated at a maximum depth of either 100 or 200 nm. On the Triboindenter, loading was terminated at 250 and 1000 μN, as it was not possible to terminate loading at a specific depth; these maximum loads were chosen to attain approximately the same maximum depth of indentation as on the NanoTest600. In both sets of experiments, a constant loading/unloading rate of 20 μN/s was applied, and a dwell period of 10 s was imposed at the maximum load, prior to unloading. By employing each indenter as a scanning probe, the accuracy of indenter positioning at the center of the lines was better than ±0.1 μm. All indentations were oriented identically with respect to the line direction in order to minimize anisotropic effects due to the low symmetry of the Berkovich (trigonal pyramid) indenter. Figure 1 shows a series of large indentations at the center of the top surface of a 3-μm-wide line to demonstrate positioning accuracy.

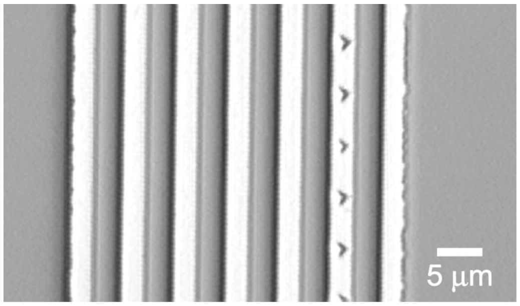

FIG. 1. Micrographs of a series of indents at the center of the top surface of a 3-μm-wide Al line on a Si substrate. The maximum depth of indentation was 500 nm to demonstrate large indents. All indentations were oriented in the same way with respect to the line direction.

B. Nanoindentation results for continuous films

Characteristic discontinuities, which have been observed consistently in the experimental $P-h$ responses of thin film or bulk single- and polycrystalline face-centered-cubic (fcc) metals indented to nanometer-scale depths,[7,9] are also observed in this study. The initial portion of the $P-h$ curves prior to the first discontinuity follows the elastic response for spherical indentation.[12] At the onset of the first discontinuity, the estimated local shear stresses beneath the indenter, approach the theoretical strength of Al ($\mu/10=2.7$ GPa, where μ is the shear modulus). This observation indicates that homogeneous defect nucleation is a plausible mechanism for the initiation of contact-induced plasticity.[10,11] After deviation from the initially elastic response, the $P-h$ response gradually approaches the prediction of sharp indentation for an elastoplastic material. For a film of 1 μm thickness, the penetration depth at a load of 200 μN is less than 10% of the film thickness t, a generally accepted depth limit[14] beyond which the substrate may contribute to the nanoindentation response of the films. Up to this loading point, however, the $P-h$ response consists of a series of discontinuities, and the transition to the continuous elastoplastic response is not at-

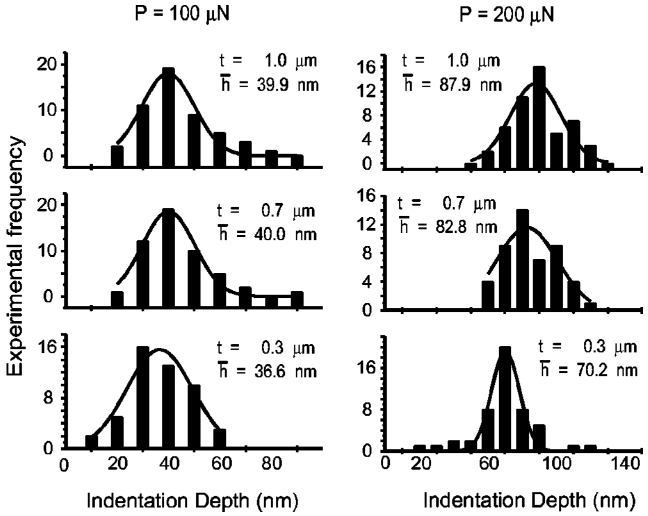

FIG. 2. Statistical distributions of indentation depth at 100 and 200 μN indentation load for polycrystalline Al thin films of 0.33, 0.7, and 1.0 μm thicknesses. Each set of experiments contained 50 indentations. The mean penetration depths of indentation $\overline{h}=h_{\mathrm{mean}}$ are indicated near the normal distribution curves, which are denoted by the solid lines. The indenter tip radius $R=500$ nm.

tained fully. Due to the presence of these discrete events in the $P-h$ response, these data cannot be analyzed in terms of continuum concepts of plasticity.

In order to analyze the discontinuous nanoindentation response quantitatively, the penetration depth h, at a particular level of imposed load P, is considered as a measure of the indentation compliance of the material during nanoindentation. This parametrization can be extended to nanoindentation of patterned lines, where the general analysis of indentation based on the semi-infinite half space of the indented material is invalid due to the unconstrained line sidewalls. These loads are chosen to be 100 and 200 μN, such that the corresponding indentation depths are less than $0.10t$ in a continuous film where $t=1$ μm.

Figure 2 shows the statistical distribution of penetration depths of continuous thin Al films at fixed indentation loads of 100 and 200 μN. The mean penetration depths h_{mean} are also indicated. Although there exists a relatively large scatter in experimental data, likely due to the polycrystalline nature and as-prepared surface roughness of the specimens, the observed trend is clear: thicker films are more compliant under the same indentation load, resulting in a greater indentation depth. Results observed with a sharper indenter tip ($R \sim 100$ nm) show the same trend. At a load of 100 μN, the average penetration depths h_{mean} of 0.7- and 1.0-μm-thick films are the same, but exceed that of the 0.33-μm-thick film, indicating no thickness effect on the $P-h$ response at this load for $t>0.7$ μm. The variation of penetration depths (i.e., experimentally observed scatter) is similar for all three films, with the exception that the two thicker films exhibit an increased frequency of above-average penetration depths. Note that at a load of 200 μN, the mean penetration depth and the distribution of observed depths (scatter) increase with increasing t.

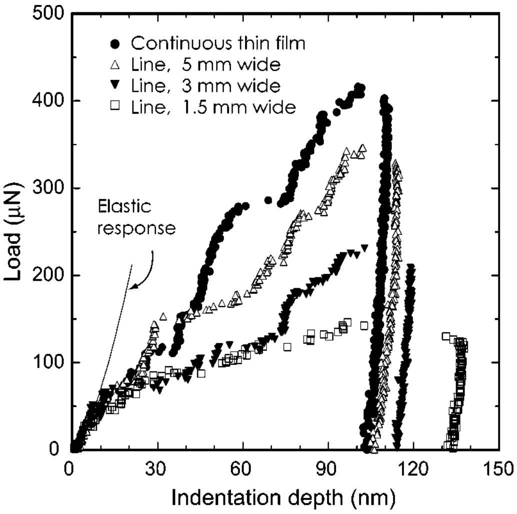

FIG. 3. Load–displacement ($P-h$) responses of polycrystalline Al thin film and lines of 1.5, 3.0, and 5.0 μm linewidths. The solid line denotes the elastic response on aluminum of a spherical diamond indenter with $R=500$ nm.

C. Nanoindentation results for patterned lines

Typical load–displacement ($P-h$) responses of continuous film and patterned lines of three different linewidths, all of equal thickness t, are shown in Fig. 3. Nanoindentation was conducted with a rounded tip. The initial elastic $P-h$ response matches well with the elastic response for a spherical indentation[12] when the spherical tip radius is assumed to be 500 nm.[15] The initial deviation from the elastic response, which occurs over a load range of 45–65 μN, is approximately independent of linewidth w. The corresponding maximum shear stress sustained by the indented film and lines are 1.8–2.0 GPa at the point of first deviation from the elastic response, which compares well with the theoretical shear strength of Al ($\sim$2.7 GPa), and is similar to the trends documented for continuous films of Al and Cu.[8,9] The indentation compliance, which can be represented by the curvature of the loading response, is also unaffected by linewidth prior to the first deviation.

Each of these $P-h$ curves exhibits discontinuities (bursts) in the load–displacement response after the initial deviation from the elastic response, as observed for continuous thin films. In contrast to the elastic response, the $P-h$ response subsequent to this initial deviation is a function of w. The curvature of the loading response decreases with decreasing w, indicating that narrower lines deform more readily than wider lines. The discrete discontinuities in the $P-h$ response are not as clear as those observed in the indentation of single crystal, continuous films.[8,9] The penetration depth during a holding period of 10 s at maximum load also increases with decreasing linewidth. The unloading slope in Fig. 3 is similar for all linewidths, which results in a decrease of the apparent elastic contact modulus during unloading.

Figure 4 shows the statistical variation of indentation depths of the continuous thin film and lines of the same thickness t at fixed indentation loads of 100 and 200 μN. The mean penetration depths h_{mean} are indicated in Fig. 4. It is

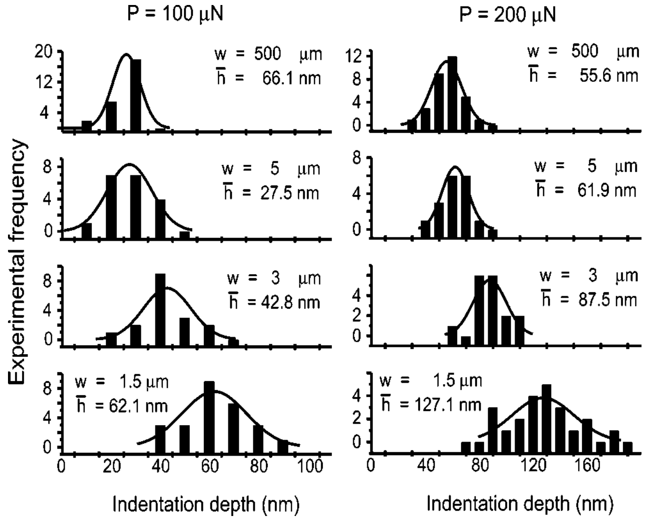

FIG. 4. Statistical distribution of indentation depth at 100 and 200 μN indentation loads for polycrystalline Al thin film and lines with 1.5, 3.0, and 5.0 μm linewidths. The mean penetration depths of indentation h_{mean} are indicated near the normal distribution curves, which are denoted by the solid lines.

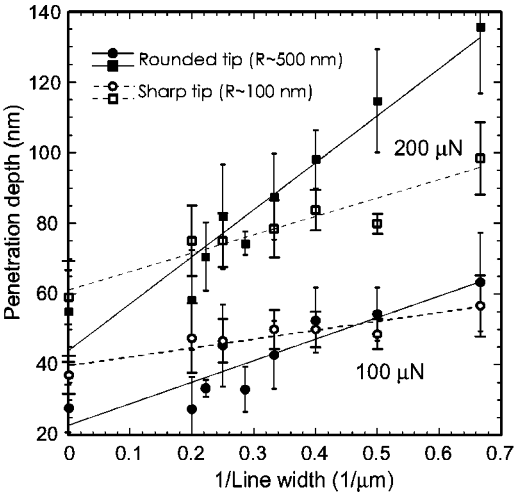

FIG. 5. Indentation depth as a function of line width for 100 and 200 μN indentation loads. The error bars indicate ±1 standard deviation in penetration depth of indentation experiments.

evident that narrower lines deform more readily under the same indentation load, resulting in a greater indentation depth (h_{mean} increases as w decreases). The variation of indentation depths in a given set of experiments for a particular linewidth increases as the linewidth decreases. Indentation penetration depths for both rounded and sharp indenter tips as a function of w for 100 and 200 μN indentation loads are summarized in Fig. 5. Each data point is the average of at least 13 experiments for a rounded tip ($R \sim 500$ nm), and of seven experiments for a sharp tip ($R \sim 100$ nm). It is apparent that the compliance increases more rapidly with decreasing w as R increases.

III. COMPUTATIONAL SIMULATIONS OF NANOINDENTATION

A. Finite element modeling

Due to the complexity of the three-dimensional (3D) elastoplastic nanoindentation problem, finite element modeling has been used extensively to simulate material response.[16,17] For bulk materials, comprehensive theoretical and computational studies have been conducted in order to infer deformation mechanisms during indentation and to extract material properties from indentation experiments.[13,16,18] For thin films and lines, however, these semiempirical solutions are generally not feasible due to additional constraints such as the film/substrate interface and the free sidewall surface of patterned lines. In such cases, FEM has been used chiefly to estimate mechanical properties by applying appropriate boundary conditions and fitting experimental data.[19,20]

Finite element models used here comprise a three-dimensional indented body and a conical rigid indenter with a spherical tip of $R = 100$ nm. The validity of the conical indenter geometry to simulate pyramidal indenters such as the Berkovich geometry has been verified by others.[16,20] The included half angle of the indenter was chosen to be 70.3° to have the same ratio between projected area and indentation depth as a pyramidal Berkovich indenter. The specimen was modeled only in a quarter space using eight-noded linear, reduced integration elements (~16 000 elements). Appropriate boundary conditions were imposed (e.g., sidewalls of the lines are free to displace normal to the sidewall surfaces), and the semi-infinite nature of the substrate was achieved by a 40×40×40 μm system size (the relative length as compared to the tip radius). Repeated simulations showed that a system that was larger than 25 μm in all directions was sufficiently large to eliminate edge effects from the fixed bottom surface of the system. The region of fine mesh near the contact area was designed to ensure numerical accuracy. The element size increased with increasing distance from the indentation axis and surface. Computations were performed using the general-purpose finite element package ABAQUS.[21] The quarter-space three-dimensional mesh was verified against the axisymmetric model for the continuous film case. Large deformation theory and frictionless contact between the indenter and material were assumed throughout the analyses.

Indentation was simulated via a complete, displacement-controlled loading and unloading cycle. The von Mises yield criterion was applied to determine the onset of plastic deformation. All film and line materials were modeled as isotropic, elastic/perfectly plastic solids, where the elastic properties were fixed to represent aluminum ($E = 70$ GPa, $\nu = 0.33$) and yield stress σ_y was varied to test hypotheses regarding deformation; perfect plasticity was assumed for mathematical simplicity. The properties of the Si substrate were fixed as a fully elastic solid ($E = 130$ GPa, $\nu = 0.28$).

B. Results of FEM simulations

FEM calculations for the load–displacement ($P-h$) responses of continuous films on Si substrates were carried out to illustrate the effect of the substrate (Fig. 6). The film thickness was fixed at 1 μm, and the maximum indentation depth was 0.2 μm. The corresponding $P-h$ responses of bulk materials with the same yield stress and a typical experimental result of a continuous polycrystalline Al film of 1 μm thick-

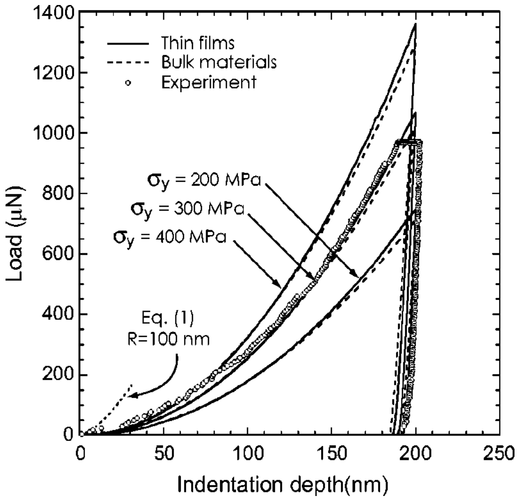

FIG. 6. Simulated $P-h$ response of 1-μm-thick Al films on Si substrates and bulk counterparts with the same yield stress. A typical experiment of a 1-μm-thick Al film on a Si substrate is also plotted.

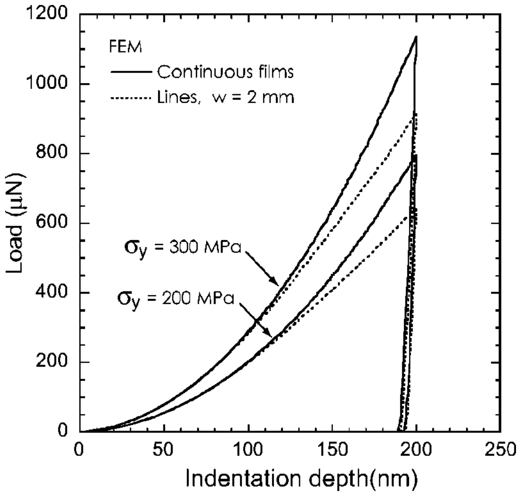

FIG. 7. Simulated $P-h$ response of continuous films and patterned lines of 2 μm width on a Si substrate. Thickness of film and lines are both 1 μm.

ness on a Si substrate are also shown in Fig. 6. As seen in Fig. 6, the associated load at a given depth of penetration increases as the yield stress increases. At the early stages of indentation, the loading portions of $P-h$ responses are essentially indistinguishable up to ~120 nm of penetration depth $(0.12t)$ for films and their bulk counterparts. Moreover, the depth at which the film and bulk cases diverge increases slightly for the softer film. A typical experimental $P-h$ curve, which was conducted by using a nominally sharp Berkovich indenter $(R\sim 100\,\text{nm})$, agrees well with the simulated curve of $\sigma_y = 300\,\text{MPa}$ beyond the early stage of indentation, in which the $P-h$ response is dominated by a series of discontinuities.

Figure 7 shows the simulated $P-h$ responses with a conical indenter $(R=100)$ on the continuous films $(t=1\ \mu\text{m})$, as well as on 2-μm-wide lines of the same thickness on a Si substrate. The yield stress of the films and the lines is assumed to be 200 and 300 MPa. The $P-h$ responses of the films and the lines with the same yield stress are essentially indistinguishable up to the loads of 200–300 μN, such that differences may not be perceptible in practice due to experimental scatter. The corresponding penetration depths are approximately 10% of the thickness.

Effects of different constraints on the early stages of $P-h$ responses cannot be rationalized via FEM simulations unless the appropriate change of the yield properties is applied, since the difference in the initial curvature of $P-h$ responses with yield stress is apparent. Such a difference was not observed in experiments due to the significant number of discontinuities in the $P-h$ responses, which is related to the discrete motion of dislocations during the transition from elastic to the plastic response. The effect of tip radius on the $P-h$ response of a continuous film and a 2-μm-wide line of the same 1 μm thickness was also simulated with yield stress of 300 MPa for both the film and the 2-μm-wide line. The $P-h$ response of the line begins to deviate at an indentation load of 300 μN, regardless of tip radius. That is, the penetration depth at a given load is not a strong function of R for the lines.

C. Molecular dynamics simulations

Atomistic simulations such as molecular dynamics calculations of nanoindentation can simultaneously provide details of the evolving defect characterization and load–displacement $(P-h)$ response over a well-defined, though limited, time period. Several researchers have modeled nanoindentation of 3D, fcc single crystals and observed discrete dislocation activity.[22–25] However, the length and time scales in such studies are limited by computational resources, resulting in unrealistic system dimensions and strain rates which are incongruous with those attainable in experiments. Despite these limitations, MD can be used to assess the effects of boundary conditions on atomistic processes such as dislocation plasticity, and is particularly well suited to the investigation of small volume structures such as patterned lines.

Two- (2D) and three-dimensional (3D) MD simulation results are presented to demonstrate the effects of size and constraints on the early stages of nanoindentation. The goal of the subsequent section is to understand qualitative trends in nanoindentation experiments by simulating $P-h$ responses in a model crystal, rather than to duplicate the exact experimental results. Thus, various simulation sizes and constraints (boundary conditions) are imposed on the MD simulation to examine the corresponding effects on the nanoindentation response (the first and subsequent discontinuities) in a 2D model crystal. Then, nanoindentation on a 3D fcc metallic crystal is simulated to extend and verify the trends extracted from the 2D simulation results. Details of the simulation are described in Refs. 11 and 26. In all simulations, indentation proceeded in displacement control. Thus, discontinuities in the $P-h$ response appear as sharp decreases in load, rather than as large bursts in displacement.

D. Results of 2D MD simulation

Two-dimensional crystals were constructed from a portion of $\underline{\text{a}}$ $\{111\}$ plane, and indentation was performed along the $\langle 112\rangle$ direction. The maximum indentation depth was

TABLE I. Conditions of molecular dynamics simulation for 2D crystals.

Code	w^a	t^a	No. of atoms	R^a	PBC[b]
F1R1	414	234	108,000	29	On
F2R1	324	156	72,000	29	On
F3R1	324	78	36,000	29	On
L1R1	324	156	72,000	29	Off
L2R1	234	156	52,000	29	Off
L3R1	171	156	38,000	29	Off
F2R2	324	156	72,000	87	On
L1R2	324	156	72,000	87	Off
L2R2	234	156	52,000	87	Off

[a] w=linewidth, t=film/line thickness, and R=indenter tip radius are given in reduced units of $[r_c]$.

[b] PBC=periodic boundary condition.

less than 10% of the film thickness t. The motion of atoms in the bottom layer was fixed, implementing the rigid film/substrate interface boundary condition. The interface was parallel to the $\langle 110\rangle$ direction. In-plane periodic boundary conditions (PBCs), perpendicular to the indentation direction, were imposed for nanoindentation of films, and were deactivated for nanoindentation of lines to allow the free motion of atoms on the surface of the line sidewall. A vacuum environment surrounded the simulation cell, and the temperature was 0 K, as maintained via a Berendsen thermostat.[27] The interatomic potential employed was a short-range, smooth cutoff analytic function chosen for its mathematical simplicity,[26] and does not reflect the interatomic potential of Al. The simulation setup and boundary conditions are summarized in Table I.

Figure 8(a) shows the change in far-field indentation load as a function of the simulation cell thickness, which represents the film thickness. The cutoff distance r_c and maximum binding energy (well-depth) ϵ of the interatomic potential are used as the primary length and energy units.[26] The equilibrium interatomic distance $r_0=0.9[r_c]$. The indenter is cylindrical with a radius $R=29[r_c]$. For both of the thicker films simulated ($t=185[r_c]$ and $234[r_c]$), the initial elastic responses are almost identical up to the second dislocation burst. The critical indentation load for the first homogeneous defect nucleation event is $2100[\epsilon/r_c]$ at an applied depth of $5.73[r_c]$. The corresponding maximum shear stress underneath the cylindrical indenter is $45.4[\epsilon/r_c^2]$, which is 13% of the calculated shear modulus[26] $(\mu=2\sqrt{3}/(1-r_0)^2=346.4[\epsilon/r_c^2])$, and is close to the estimated theoretical shear strength of this model material, $(\tau_c=\mu/(2\pi)=55.1[\epsilon/r_c^2])$. Note that the units of stress are $[\epsilon/r_c^2]$ because this is a 2D system. It is verified that each load relaxation in Fig. 8(a) corresponds to a sequence of dislocation dipole nucleation through the visualization of the atomic coordination number. The deviation of the thinnest film case ($t=78[r_c]$) from the predicted elastic response arises from a strong substrate effect: the stress field imposed by the indenter approaches the film/substrate interface even prior to the first observed discontinuity.

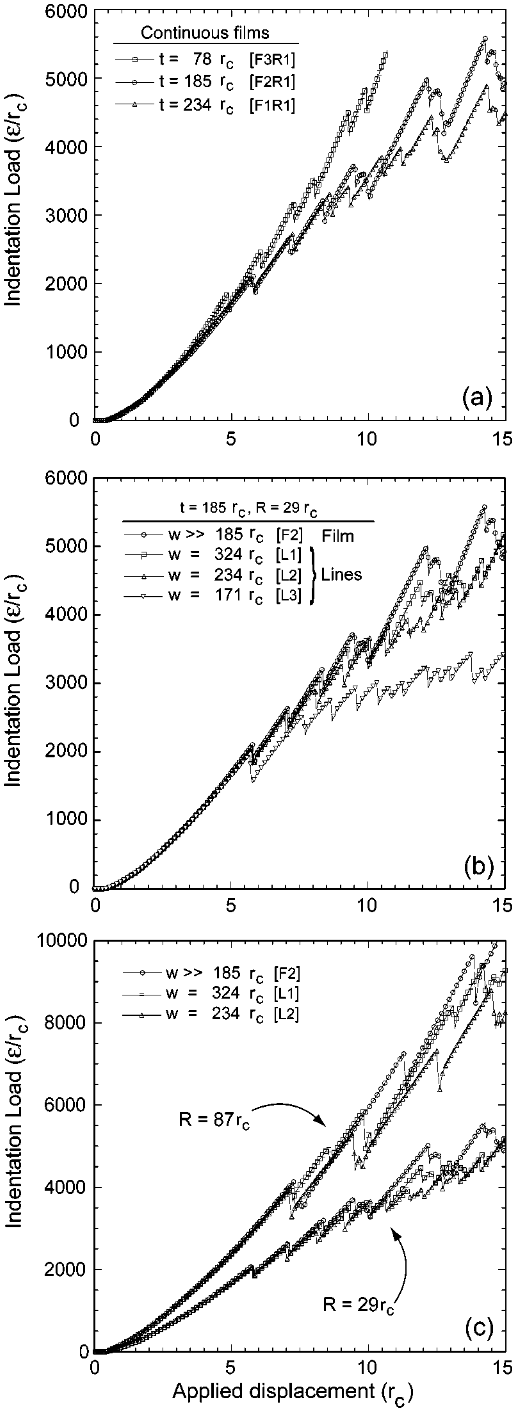

FIG. 8. MD simulated $P-h$ responses. All units are in reduced units, with load as $[\epsilon/r_c]$ and depth as $[r_c]$. (a) Effect of film thickness. $R=29[r_c]$; (b) effect of linewidth. $R=29[r_c]$; and (c) effect of tip radius. The simulations are conducted on a film and lines of two widths with $R=29[r_c]$ and $87[r_c]$.

After the first load relaxation, which corresponds to subsurface dislocation dipole nucleation, the dislocation dipole separates. One dislocation moves to the surface, making a surface step, and the other quickly moves into the material. Once a dislocation nucleates and moves away, the local stress (i.e., the stress in the region near the position of dipole nucleation) decreases by a certain amount, which relates to the relaxation in the far-field external load. The force balance determines the equilibrium position of the dislocation. The force imposed on the dislocation includes the repulsive stress field imposed by the indenter and the repulsive stress field due to the elastic mismatch at the film/substrate interface. Due to the fixed position of the bottom layer, the imaginary substrate has an infinitely large elastic modulus, which repels the dislocation from the interface. In order to nucleate subsequent dislocations homogeneously, the local stress must increase again to the GPa level. As the contact width increases (i.e., as indentation depth increases), the load required to reach this stress level increases. In addition, since the previously nucleated dislocation exerts a stress field on the region of maximum shear stress beneath the indenter, the external loading to create another dislocation is altered by the back stress of this preexisting dislocation. Therefore, thinner films sustain larger external loads subsequent to the first dislocation nucleation event because of greater back stress: Increased proximity of the (repulsive) substrate interface causes previously generated dislocations to remain closer to the indenter tip. The overall load–displacement relation becomes less compliant when the film thickness decreases, as the film effectively hardens more readily.

The effect of linewidth on the MD simulated $P-h$ response is illustrated in Fig. 8(b). As expected, soon after the first deviation from the elastic behavior occurs, the indentation responses show increasing compliance with decreasing linewidth. Unlike the effect of film thickness, the elastic responses prior to the first deviation are the same for all three linewidths because the initial stress field does not approach either the substrate interface or the free surface of the line sidewall. The effect of linewidth is evident in subsequent $P-h$ responses after several dislocations have been generated and have moved away from the indenter tip. As argued above, the back stress from the previously generated dislocations alters the far-field external loading, and, in the case of lines, the free surface of the line sidewall decreases the effective back stress from dislocations to the indenter tip. In these lines, dislocations move to the free surface to relieve the external loading stresses, rather than to the substrate interface where they contribute to back stresses that would increase the external loading required for further deformation.

The MD simulated $P-h$ responses of films and lines of two distinct widths are illustrated for the indenter tip radii of $R=29[r_c]$ and $R=87[r_c]$ in Fig. 8(c). The maximum shear stresses at the first dislocation nucleation events are $45.7[\epsilon/r_c^2]$ and $36.7[\epsilon/r_c^2]$ for $R=29[r_c]$ and $R=87[r_c]$, respectively, which are 13% and 11% of the shear modulus $\mu=346.4[\epsilon/r_c^2]$. Note that compliance increases with decreasing linewidth, in agreement with our experiments. That is, as the linewidth decreases, so does the overall resistance of the yielding structure to further plastic deformation, resulting in an inverse relationship between penetration depth and line width for a given load. This result is not predicted for a continuous film or bulk material, and appears to be due to the reduction in dislocation back stress afforded by movement of dislocations to the free sidewalls of the line. Note further that the compliance increases more rapidly with decreasing line width when R is larger, as is consistent with our experimental observations. In continuous films and bulk samples analyzed via continuum mechanics, increasing R correlates with decreasing stress for a given indentation load, and thus compliance decreases with increasing R. This contrast points to the interaction between the boundary conditions and the indentation stress field: As the plastic zone of indentation approaches the dimensions of the line, the sidewalls facilitate stress relaxation and the line deforms more readily than film or bulk counterparts.

E. Results of 3D MD simulations

Although 2D molecular dynamics simulations can afford insight into the initial stages of nanoindentation and the effects of various constraints, these computations cannot be compared directly to experimentally observed nanoindentation behavior because (1) dislocation structure is limited to [one-dimensional (1D)] edge dislocations; (2) the restricted dimensionality of these dislocations confers artificially high mobility; and (3) the $P-h$ response does not converge (i.e., it is dependent on the size of the sample). Previous 3D MD simulations[11] have shown that dislocations and defects intersect to form complex structures beneath the indenter tip, including the formation of sessile locks due to the concurrent nucleation of dislocations on adjacent slip planes in Al subject to spherical nanoindentation. These sessile locks can serve as heterogeneous nucleation sites for defects in the subsequent stage of nanoindentation. Thus, to extend 2D simulations, 3D MD simulations of spherical indentations have been performed for a spherical indentation of Cu comprising 90 000 atoms. We chose to model Cu rather than Al because the accuracy of the Mishin Cu embedded atomic potential[28] at large strains has been confirmed independently.[29] However, it should be noted that the stacking fault energy and elastic anisotropy of Al and Cu differ substantially. A sphere of 4 nm radius was used to indent normal to the $\{111\}$ plane of the defect-free Cu single crystal in displacement control. The simulation size was $8.85\times9.39\times12.78$ nm in x, y, and z directions, respectively. The displacement rate of the indenter was 12 m/s along the negative y direction. The bottom of the $y=0$ plane was fixed to simulate a rigid substrate. The periodic boundary conditions along the x direction were deactivated to simulate the patterned line structure of the same dimension.

Figure 9 shows the $P-h$ response of the system with and without PBCs along the x direction, which represent a continuous film and a patterned line on a substrate, respectively. In all simulations, the initiation of dislocation activity was concurrent with far-field indentation load relaxation, and the dislocation structure comprised dislocation glide loops on $\{111\}$ slip planes. As expected, the indentation response is identical for both cases, up to the first load relaxation (i.e., within the elastic regime). After the first deviation from the elastic response, dislocations nucleate inside the material near the top surface and generate loops in the $\{111\}$ slip planes. Further load relaxation is mediated by expansion of these glide loops in the slip planes. The expanding glide loops intersect the surface, and generate $\langle 110\rangle$ slip steps. The subsequent $P-h$ response indicates clear differences in the behavior of the film and line cases. The defect structure underneath the indenter is shown for both cases in Fig. 10 at a load of 0.3 μN, corresponding to points A and B in Fig. 9.

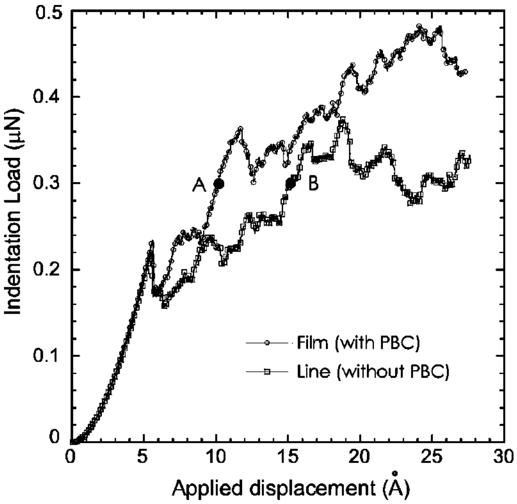

FIG. 9. MD simulated load–displacement ($P-h$) responses of 3D Cu crystal comprising 90 000 atoms. A sphere of 0.4 nm radius indents normal to the {111} plane of the defect-free crystal of Cu. The simulation size is 8.85 nm×9.39 nm×12.78 nm. The displacement rate of the indenter is 12 m/s.

Atoms having the perfect bulk coordination number, 12, are not shown for ease of visualization. For the film case, those dislocations generated by the contact are entangled beneath the contact area. The density of defects is higher than that of the line case, which results in a higher rate of strain hardening during indentation loading. In contrast, the volume of the defect structure for the line case is larger (i.e., lower defect density), and some dislocations escape from the free surface of the line sidewall and form several ⟨110⟩ slip steps. Note that the presence of these sidewall slip steps correlates with the decreased density of dislocations beneath the contact zone and on the top surface of the line (compared to the film case), facilitating a relative increase in the penetration depth sustained by the line structure. The anisotropy of such slip step formation may be related to the elastic anisotropy of the Cu crystal.

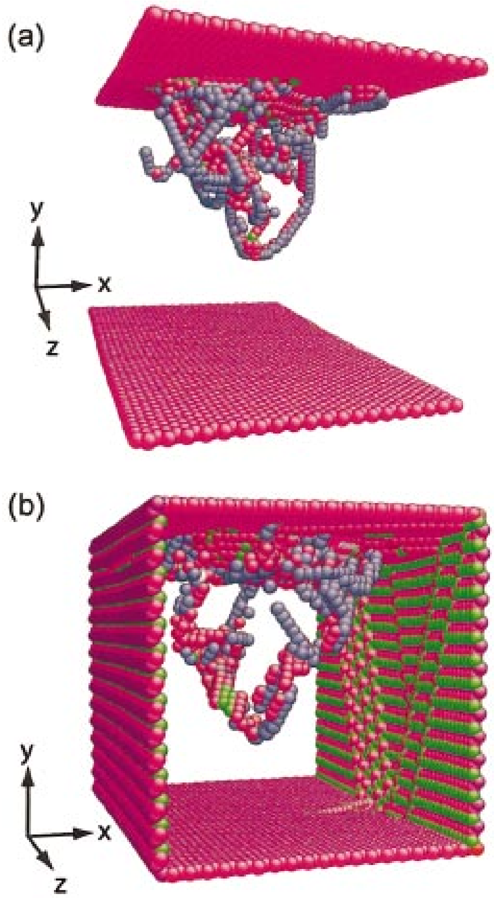

FIG. 10. (Color) Defect structures underneath indenters for (a) the film case and for (b) line case at a load of 0.3 μN (denoted as points A and B in Fig. 9). In both cases, $x=\langle 11\bar{2}\rangle$, $y=\langle 111\rangle$, and $z=\langle 1\bar{1}0\rangle$.

IV. DISCUSSION

Both theoretical and experimental studies for thin metal films on a substrate, chiefly via curvature and x-ray diffraction methods, have shown that a thinner film is plastically stronger (less compliant) than a thicker one.[4] In this case, a homogenous state of equibiaxial stress exists in the thin film (except near the free edges). In contrast, the stress field near the indenter tip is highly localized and inhomogeneous. Several studies have investigated the influence of substrates on the nanoindentation responses of thin films.[19,30–32] The chief concerns of these investigations have been estimation of the hardness and modulus of films independent of the substrate. As these studies employed continuum analysis and focused on the unloading response required to calculate these material parameters, such findings cannot be extended directly to our experimental observations which are dominated by discrete load–displacement events. In addition, the indentation depths considered in the present study were about 12% of film thickness. Ohmura *et al.*[33] experimentally verified that the critical depth, beyond which the substrate contributes to the $P-h$ response, can be extended 20% of film thickness for several fcc metal thin films on sapphire single crystal. Recent finite element modeling showed that the limits can be extended to greater depth for softer films on harder substrates.[32] Therefore, it is likely that the change of indentation compliance with film thickness, especially in the thicker films used in the present experiments ($t=0.7$ and 1.0 μm), is not attributable to an increasing yield stress with decreasing film thickness. Moreover, the present experimental observation of nanoindentation on patterned lines showed that narrower lines deform more readily under nanoscale contact. Although the properties of patterned lines are much less explored, this observation suggests that the effective yield stress may decrease with decreasing linewidth. FEM-simulated $P-h$ responses of patterned lines with the same yield stress as the continuous film have failed to explain such a large increase in compliance under indentation (Fig. 7). However, the significant number of discontinuities in the very early stages of indentation responses, which relate to the discrete motion of dislocations, prevents straightforward interpretation of the increase in compliance of lines with decreasing σ_y.

The simulation results from the previous section indicate that the continuum approach via FEM has a limited use in rationalizing nanoindentation experiments in which the discrete discontinuities are dominant. Although FEM can consider more realistic dimensions, and the quasistatic nature of nanoindentation loading, the simulated indentation responses are insufficient to reproduce the overall experimental trends at the nanoscale, whereas MD simulations of 2D perfect crystals clearly exhibit the general trends observed experimentally. However, the mobility of dislocations in 2D crystals is artifactually high due to the lack of out-of-plane constraints, and the number of dislocations examined is quite low ($\leqslant 20$), compared to the number expected in the real experiments (>150). In 3D simulations, the cluster of defects expanded much more in the lateral directions than observed in 2D simulations, due to the entanglement of concurrently generated dislocations in adjacent slip planes. Some of these dislocations indeed escaped to the line sidewall, and facilitated penetration of the indenter by depositing slip steps in addition to those on the top surface of the line. Consequently, the size of the defect zone, or volume occupied by defects, is larger in the patterned line than in the continuous film. Beyond the region of discontinuities, continuum approaches should prevail, a feature which has already been validated by others.[16,20] It should be noted that there is no effect of geometrical constraints on the elastic response of nanoindentation prior to the first discontinuity in this small scale deformation.

V. CONCLUSIONS

In this work, systematic investigation of size scale effects on the early stages of nanoindentation-induced plasticity has been conducted via experimental and computational approaches. It is evident that there is no size effect on the elastic load–displacement ($P-h$) responses. Beyond the onset of plasticity, two size scales (film thickness and linewidth) exhibit distinct effects on the $P-h$ responses, depending on their geometric constraints; the bottom of the films is constrained by the film/substrate interface, but the sidewall surfaces of the lines are free to deform. The indentation penetration depth decreases as the film thickness decreases (plastically less compliant) for the continuous films, whereas the penetration depth increases as the linewidth decreases (plastically more compliant) for the patterned lines.

Through computational simulations with concomitant experimental observations of nanoindentation, we have shown that the early stage plasticity of small volume structures is described more accurately by discrete dislocation interactions than by continuum concepts. These results indicate that individual defects and their interaction with boundary conditions become important in this extremely small-scale deformation, and that the stress arising from those defects counters the far-field applied load. The resistance to indenter penetration is determined by the force balance between the applied stress field imposed by the indenter and the stress field imposed by the dislocations in their equilibrium position. For continuous films, increased proximity to the film/substrate interface (decreasing film thickness) causes greater resistance to the indenter penetration due to the repulsive stress field of previously generated dislocations by the elastic mismatch at the interface. In contrast, the existence of free sidewall surfaces in patterned lines reduces this repulsive stress field. Under these reduced constraints, dislocations relieve stress due to external loading by terminating at the sidewall surfaces, resulting in greater penetration depth of indentation and an apparent increase in plastic compliance.

ACKNOWLEDGMENTS

This work was supported by the Defense University Research Initiative on NanoTechnology (DURINT) on ‘‘Damage- and Failure-Resistant Nanostructured and Interfacial Materials,’’ which is funded at the Massachusetts Institute of Technology (MIT) by the Office of Naval Research under Grant No. N00014-01-1-0808.

[1] M. Ohring, *The Materials Science of Thin films* (Academic, San Diego, 1991), pp. 407–409.
[2] H. Huang and F. Spaepen, Acta Mater. **48**, 3261 (2000).
[3] E. Arzt, Acta Mater. **46**, 5611 (1998).
[4] L. B. Freund and S. Suresh, *Thin Film Materials* (Cambridge University Press, Cambridge, U.K., 2003).
[5] R. Vinci, O. Kraft, N. Moody, P. Besser, and E. Shaffer II (eds.) Mater. Res. Soc. Symp. Proc. **594** (1999).
[6] W. D. Nix, Metall. Trans. A **20A**, 2217 (1989).
[7] D. F. Bahr, D. E. Kramer, and W. W. Gerberich, Acta Mater. **46**, 3605 (1998).
[8] S. Suresh, T. G. Neih, and B. W. Choi, Scr. Mater. **41**, 951 (1999).
[9] A. Gouldstone, H. J. Koh, K. Y. Zeng, A. E. Giannakopoulos, and S. Suresh, Acta Mater. **48**, 2277 (2000).
[10] A. Gouldstone, K. J. Van Vliet, and S. Suresh, Nature (London) **611**, 656 (2001).
[11] J. Li, K. J. Van Vliet, T. Zhu, S. Yip, and S. Suresh, Nature (London) **418**, 307 (2002).
[12] K. L. Johnson, *Contact Mechanics* (Cambridge University Press, Cambridge, U.K., 1985).
[13] W. C. Oliver and G. M. Pharr, J. Mater. Res. **7**, 1564 (1992).
[14] G. M. Pharr and W. C. Oliver, MRS Bull. **17**, 28 (1992).
[15] Y. Choi and S. Suresh, Scr. Mater. **48**, 249 (2003).
[16] M. Dao, N. Chollacoop, K. J. Van Vliet, T. A. Venkatesh, and S. Suresh, Acta Mater. **49**, 3899 (2001).
[17] Y. T. Cheng and C. M. Cheng, J. Appl. Phys. **84**, 1284 (1998).
[18] M. F. Doerner and W. D. Nix, J. Mater. Res. **1**, 601 (1986).
[19] A. K. Bhattacharya and W. D. Nix, Int. J. Solids Struct. **24**, 1298 (1988).
[20] J. A. Knapp, D. M. Follstaedt, S. M. Mayer, J. C. Bardour, and T. A. Friedmann, J. Appl. Phys. **85**, 1460 (1999).
[21] *ABAQUS Version 6.1: General Purpose Finite Element Program* (Hibbit, Karlson, and Sorensen, Pawtucket, RI, 2000).
[22] J. A. Zimmerman, C. L. Kelchner, P. A. Klein, J. C. Hamilton, and S. M. Foiles, Phys. Rev. Lett. **87**, 165507 (2001).
[23] J. D. Kiely and J. E. Houston, Phys. Rev. B **57**, 588 (1998).
[24] C. L. Kelchner, S. J. Plimpton, and J. C. Hamilton, Phys. Rev. B **58**, 11085 (1998).
[25] E. T. Lilleodden, J. A. Zimmerman, S. M. Foiles, and W. D. Nix, J. Mech. Phys. Solids **51**, 901 (2003).
[26] K. J. Van Vliet, J. Li, T. Zhu, S. Yip, and S. Suresh, Phys. Rev. B **67**, 104105 (2003).
[27] H. J. C. Berendsen, J. P. M. Postma, W. F. van Gunsteren, A. DiNola, and J. R. Haak, J. Chem. Phys. **81**, 3684 (1984).
[28] Y. Mishin, M. J. Mehl, D. A. Papaconstantopoulos, A. F. Voter, and J. D. Kress, Phys. Rev. B **63**, 224106 (2001).
[29] T. Zhu, J. Li, K. J. Van Vliet, S. Suresh, and S. Yip, J. Mech. Phys. Solids (in press).
[30] T. Y. Tsui and G. M. Pharr, J. Mater. Res. **14**, 292 (1999).
[31] R. Saha and W. D. Nix, Acta Mater. **50**, 23 (2002).
[32] X. Chen and J. J. Vlassak, J. Mater. Res. **16**, 2974 (2001).
[33] T. Ohmura, S. Matsuoka, K. Tanaka, and T. Yoshida, Thin Solid Films **385**, 198 (2001).